

QUASARS AS A TRACER OF LARGE-SCALE STRUCTURES IN THE DISTANT UNIVERSE

HYUNMI SONG¹, CHANGBOM PARK¹, HEIDI LIETZEN^{2,3} AND MARET EINASTO⁴*Draft version March 5, 2024*

ABSTRACT

We study the dependence of the number density and properties of quasars on the background galaxy density using the currently largest spectroscopic datasets of quasars and galaxies. We construct a galaxy number density field smoothed over the variable smoothing scale of between approximately 10 and $20 h^{-1}\text{Mpc}$ over the redshift range of $0.46 < z < 0.59$ using the Sloan Digital Sky Survey (SDSS) Data Release 12 (DR12) Constant MASS (CMASS) galaxies. The quasar sample is prepared from the SDSS I/II DR7. We examine the correlation of incidence of quasars with the large-scale background density and dependence of quasar properties such as bolometric luminosity, black hole mass, and Eddington ratio on the large-scale density. We find a monotonic correlation between the quasar number density and large-scale galaxy number density, which is fitted well with a power law relation, $n_Q \propto \rho_G^{0.618}$. We detect weak dependences of quasar properties on the large-scale density such as a positive correlation between black hole mass and density, and a negative correlation between luminosity and density. We discuss the possibility of using quasars as a tracer of large-scale structures at high redshifts, which may be useful for studies of growth of structures in the high redshift universe.

Subject headings: large-scale structure of universe – cosmology: observations – quasars: general

1. INTRODUCTION

Quasars are the most luminous type of Active Galactic Nuclei (AGN) with luminosity more than hundreds times higher than that of normal galaxies. Thanks to such brightness, quasars can be observed all across the universe as far as $z = 7$ (Mortlock et al. 2011; Momjian et al. 2014). Many studies of quasars have focused on discovering them and characterizing individual objects to shed light on formation and evolution of non-linear structures at high redshifts (Turner 1991; Djorgovski 1999; Djorgovski et al. 2003, 2006). In recent years, large surveys such as the Sloan Digital Sky Survey (SDSS; York et al. 2000; Gunn et al. 2006) and the 2dF QSO Redshift Survey (Croom et al. 2004), have accumulated large spectroscopic data sets of quasars. This enables us to perform statistical studies of quasars with broad scope.

Using these quasar survey data, Clowes et al. (2013), Nadathur (2013), Einasto et al. (2014) and Park et al. (2015) found very large quasar groups and discussed the cosmological implications of the existence and properties of these extreme objects. Nadathur (2013), Einasto et al. (2014) and Park et al. (2015) pointed out that Clowes et al. (2013)'s cosmological interpretation of large quasar groups that questions the validity of the cosmological assumption of homogeneity and isotropy is misleading. They stressed the importance of a statistically precise analysis to draw conclusions on cosmological implication from existence of one or a few extreme objects in observation. Park et al. (2015) also emphasized that statistical comparison with cosmological simulations must be employed as well. The quasar survey data are also used

for studies of constraining cosmological parameters (Han & Park 2015; Risaliti & Lusso 2015). Besides the studies directly related to cosmology, there are more studies of exploring quasar clustering properties. Einasto et al. (2014) made a catalog of quasar groups with different linking lengths and examined their properties. They found that the characteristics of quasar groups such as number density, size and richness, identified with linking lengths varied from 20 to $40 h^{-1}\text{Mpc}$ are well correlated with those of galaxy superclusters. Therefore such quasar groups can be markers of galaxy superclusters. As a classical way to study clustering properties, correlation functions have been measured for quasars (AGN in general) by many different groups (Krumpe et al. 2010; Miyaji et al. 2011; Krumpe et al. 2012, 2015; Cappelletti et al. 2012; Allevato et al. 2014; Shen et al. 2007b, 2009, 2013; Richardson et al. 2012; Eftekharzadeh et al. 2015; Ross et al. 2009). They have measured two-point cross-correlation functions (2PCCFs) between quasars and galaxies. They have found the typical mass of quasar-hosting dark matter halos (DMHs) and dependence of the mass on quasar luminosity.

Among the above-mentioned clustering studies, Shen et al. (2013) measured the 2PCCFs of the quasars in the catalog of Schneider et al. (2010) and the SDSS Constant MASS (CMASS) galaxies, and found that quasars at $z \sim 0.5$ live in DMHs with mass of about $4 \times 10^{12} h^{-1} M_\odot$. Even though the DMH mass gives us general information on the large-scale environments preferred by quasars (the value corresponds to the scale of galaxy groups), some environmental information, for example characterized by background density, is not explicitly readable in the 2PCCFs typically measured in AGN clustering studies. Such information can be preserved by taking a different approach from 2PCCFs, and instead determining how quasars populate the density field traced out by galaxies. Among the previous studies taking this approach, Lietzen et al. (2009) and Lietzen et al. (2011)

¹ School of Physics, Korea Institute for Advanced Study, Heogiro 85, Seoul 130-722, Korea

² Instituto de Astrofísica de Canarias, E-38205 La Laguna, Tenerife, Spain

³ Universidad de La Laguna, Dept. Astrofísica, E-38206 La Laguna, Tenerife, Spain

⁴ Tartu Observatory, 61602 Toravere, Estonia

constructed a large-scale density field, identified large-scale structures (LSSs), and found that quasars and other AGN at $z < 0.4$ are typically located in the outskirts of galaxy superclusters.

In addition to studying structures on very large scales, direct measures of the galaxy density field also allow us to explore the environmental dependence of quasar properties such as black hole mass and luminosity. It is an approach in the reverse order of that used for the 2PCF: we select quasars on the basis of their environment and examine the trend of environment-averaged properties, while the 2PCF studies select quasars on a quasar property and compute the average galaxy densities around quasar subsamples. The method used here may be more sensitive in detecting any environmental dependences than the 2PCF one. Recently, Hutsemékers et al. (2014) showed that quasar polarizations are aligned to directions of the LSS to which they belong. Pelgrims & Hutsemékers (2015) detected large-scale alignments of quasars polarization vectors. There are also studies done with cosmological hydrodynamical simulations showing that formation and evolution of galaxies are likely to be in part driven by cosmic web (Laigle et al. 2015, and references therein). Based on this range of observational and theoretical work, there is clear motivation for studying the connection between the properties of quasars and their host LSSs.

In this paper we construct a three-dimensional galaxy number density field and study the occurrence of quasar as a function of galaxy number density at $z \sim 0.5$. A three-dimensional galaxy number density field contains different information from the 2PCFs, and provides a more direct picture of LSS and matter distribution. We will use the galaxy number density field to investigate the dependence of various properties of quasars, such as luminosity, black hole mass and Eddington ratio, on the background galaxy density. It should be noted that in this paper we focus on how quasar activity is related to the local galaxy density traced by massive galaxies, rather than to the underlying local matter density. We adopt a flat Λ CDM cosmology with $\Omega_M = 0.27$, $\Omega_\Lambda = 0.73$ and $h = 0.7$, and comoving distances are used throughout the paper.

2. DATA

We use the fifth edition of the SDSS quasar catalog of Schneider et al. (2010) from SDSS DR7 which is a compilation of quasars observed by the SDSS-I/II quasar survey. The catalog contains 105783 spectroscopically confirmed quasars over a wide redshift range of $0.065 < z < 5.46$ in the area covering approximately 9380 deg^2 of the sky. They are brighter than the i -band absolute magnitude of $M_i = -22.0$ (M_i is galactic extinction-corrected and K-corrected to $z = 2$ in a cosmology with $H_0 = 70 \text{ km/s/Mpc}$, $\Omega_m = 0.3$ and $\Omega_\Lambda = 0.7$) and have at least one broad emission line with Full Width at Half Maximum (FWHM) larger than 1000 km/s or interesting/complex absorption features. They have apparent i -magnitude of $14.86 < i < 22.36$, where the bright limit comes from the maximum brightness limit of the target selection on quasar candidates to avoid saturation and cross-talk in the spectra. The catalog does not include several classes of AGN such as Type II quasars, Seyfert galaxies and BL Lacertae ob-

jects. For the details of target selection process for spectroscopic observation and quasar confirmation process, see Richards et al. (2002) and Schneider et al. (2010). The original survey of the SDSS quasars turned out to be non-uniform in the selection of targets. To remedy this problem Shen et al. (2011) evaluated the SDSS target selection and provided a so-called uniform flag in their catalog. The quasar sample is expected to be statistically uniform when only the quasars with the uniform flag equal to 1 are selected (Richards et al. 2002, 2006; Shen et al. 2007b).

To construct a large-scale galaxy density field we use the latest CMASS galaxy catalog (DR12v4; Alam et al. 2015) of SDSS-III (Eisenstein et al. 2011) Baryonic Oscillation Spectroscopic Survey (BOSS; Dawson et al. 2013; Smee et al. 2013), which contains 621849 galaxies mostly in the redshift range of $0.4 < z < 0.8$. The CMASS sample is designed to have massive galaxies to detect Baryonic Acoustic Oscillation (BAO) around $z \sim 0.5$ through a set of flux and color selection criteria. For more details about the CMASS target selection criteria, see Eisenstein et al. (2001), Cannon et al. (2006) and Bolton et al. (2012). Those massive BOSS CMASS galaxies are an optimal tracer of the large-scale matter distribution.

The stellar masses of CMASS galaxies are above $10^{11.2-11.3} M_\odot$ (Chen et al. 2012; Maraston et al. 2013). We use the group catalog of the SDSS main sample by Tempel et al. (2014) as a comparison to determine what fraction of the high-mass galaxies are central galaxies of their groups. We find that 87% of the galaxies above $10^{11.3} M_\odot$ in the distance bin from 120 to $340 h^{-1} \text{ Mpc}$ are the first-rank galaxies (most luminous) of their groups (see also Lietzen et al. 2016). In that sense, the CMASS sample does not suffer much from peculiar motions, thus we do not need to worry about contamination by galaxy peculiar motion in the galaxy density estimate. Even for 13% of non-central galaxies, the galaxy density we calculate is a value smoothed over a larger scale ($\sim 15.2 h^{-1} \text{ Mpc}$; see Section 3.2) than a typical uncertainty level due to peculiar motion of a galaxy cluster ($< 5 h^{-1} \text{ Mpc}$ in comoving scale at $z \sim 0.5$).

The BOSS CMASS sample suffers from various systematics of missing galaxies due to fiber collisions, poor or failed observations, and so on. In calculating the galaxy number density we will use a weight given to each galaxy to take the systematic effects into account. More details on the weight will be given in the next section.

To make a statistically homogeneous sample of density tracers we apply a cut to the galaxy sample in i -band absolute magnitude versus redshift space so that the comoving number density of galaxies becomes roughly constant of redshift. The cut is obtained via fitting with a functional form of

$$M_{i,\text{cut}} = 0.3 \left(\frac{\pi}{2} - \text{atan}(41.9(z - 0.459)) \right) - 22.6. \quad (1)$$

The resulting sample has the mean galaxy separation of $17.1 h^{-1} \text{ Mpc}$, which is the cube root of the typical volume occupied by each galaxy. We limit our sample within the redshift range of $0.45 < z < 0.61$, where the cut does not change drastically (meaning survey completeness guaranteed) and as many galaxies as possible can be kept while satisfying the constant number density condition.

Figure 1 shows the distributions of galaxies (left) and

quasars (right) in the northern galactic cap (NGC). To reduce the effects of sample boundaries in the calculation of local density some of the jagged boundaries of the CMASS galaxy distribution are cut off, which removes about 2% of CMASS galaxies. Galaxies located within the newly defined boundaries are shown in red and they are used to calculate the density field. In the right panel quasars having the uniform flag equal to 1 and also within a cleaned boundaries are shown in red. It is seen that the sample of quasars with the uniform flag of 1 is divided into three contiguous regions. We use the subsample in the middle that has the largest volume. Our analyses are limited within the region where the galaxy and quasar samples overlap each other. Figure 2 shows the selected galaxies and quasars for our analysis in the plane of i -band absolute magnitude and redshift with black dots. The gray dots represent those in the original samples within the NGC and cleaner boundaries.

3. GALAXY DENSITY FIELD

3.1. Calculating the smooth galaxy density field

We use a smooth number density field of the CMASS galaxies to examine how quasars are distributed relative to the LSSs of galaxies. We apply the Spline-kernel smoothing with variable kernel size to the sample of CMASS galaxies prepared as described in the previous section. We embed our sample within a large cuboid and calculate the local density at the center of each cell, which is a cube with side length of $5 h^{-1} \text{Mpc}$, following the widely used method in smoothed particle hydrodynamics (SPH) (Monaghan 1992) among many other non-parametric regression estimations (Jennen-Steinmetz & Gasser 1988). The local galaxy number density at each cell is formulated as

$$\rho = \sum_{i=1}^{N_{\text{nn}}} W(r_i, h_{\text{spl}}) \quad (2)$$

where $W(r_i, h_{\text{spl}})$ is a Spline function kernel. r_i is the distance between the cell center and its i -th nearest neighboring galaxy, and h_{spl} is a smoothing length defined as $r_{N_{\text{nn}}}/2$. N_{nn} is number of nearest neighbors used for density calculation and we choose 20. The choice of 20 is made based on the test of which value of N_{nn} efficiently reproduces a uniform distribution with less than 1% error (see Appendix for more details). r_{20} varies from a location to another reflecting the density fluctuations. The Spline function kernel we adopt here is from Monaghan & Lattanzio (1985)⁵:

$$W(r_i, h_{\text{spl}}) = \frac{1}{\pi h_{\text{spl}}^3} \begin{cases} 1 - \frac{3}{2} q_i^2 + \frac{3}{4} q_i^3; & q_i \leq 1 \\ \frac{1}{4} (2 - q_i)^3; & 1 \leq q_i \leq 2 \\ 0; & \text{otherwise} \end{cases} \quad (3)$$

where $q_i = r_i/h_{\text{spl}}$. This function satisfies accuracy, smoothness and computational efficiency requirements for the interpolating kernels with its compact support

⁵ We performed a test of comparing densities calculated with the two different Spline function kernels, W_3 and W_4 of Monaghan & Lattanzio (1985). We showed that the two densities agree well with each other and the main results of this paper are robust to the choice of a Spline function kernel.

and continuous second derivative. Please see Monaghan & Lattanzio (1985) and Monaghan (1992) for more details.

As already mentioned in Section 2, some galaxies are missing from the observation and data processing and analysis for various reasons: (1) targets that have spectroscopic redshifts in the literature (denoted as *known*); (2) targets that have a target of different type (i.e. QSO) getting a fiber allocation already within $62''$ (denoted as *missed*); (3) targets that have another CMASS target within $62''$ (denoted as *close pair* or shortly *cp*); (4) targets that were assigned fibers but after spectroscopic observation, were revealed as stars (denoted as *star*); (5) targets that were assigned fibers, observed, but did not give a reliable redshift through the pipeline for various reasons (denoted as *fail*). So (2) and (3) are the cases of fiber allocation failure, and (4) and (5) are the cases of spectroscopic observation failure.

The completeness of the CMASS galaxy catalog at a location of the sky can be quantified by

$$C_{\text{sample}} = \frac{N_{\text{gal}} + N_{\text{known}} + N_{\text{cp}}}{N_{\text{gal}} + N_{\text{known}} + N_{\text{cp}} + N_{\text{missed}} + N_{\text{fail}}} \quad (4)$$

where N_{gal} is the number of galaxies in the CMASS galaxy catalog which were assigned fibers and successfully observed with spectroscopy. Here we assume that all of objects which are missed and failed are CMASS galaxies. C_{sample} would be defined in each sector, which is an area covered by a unique set of spectroscopic tiles where the observing conditions are the same. But it is not easy to find all N 's used in Equation 4 in each sector. Rather what is given in the catalog sector-by-sector is a similar quantity,

$$C_{\text{BOSS}} = \frac{N_{\text{obs}} + N_{\text{cp}}}{N_{\text{targ}} - N_{\text{known}}} \quad (5)$$

where $N_{\text{obs}} = N_{\text{star}} + N_{\text{gal}} + N_{\text{fail}}$ and $N_{\text{targ}} = N_{\text{obs}} + N_{\text{cp}} + N_{\text{known}} + N_{\text{missed}}$. It tells how well spectroscopic observation is done.

Since N_{gal} dominates over others, there is only small difference between C_{sample} and C_{BOSS} . To compare C_{sample} and C_{BOSS} we calculate them using the information given in table 1 of Anderson et al. (2014), and find that for DR11 CMASS galaxies in northern hemisphere, $C_{\text{sample}} = 0.9999 C_{\text{BOSS}}$ in the survey area as a whole. To be more precise, we need to compare them in every sector. But the spatial variation of C_{BOSS} across different sectors is small and the CMASS targets which contribute to the sample incompleteness should be distributed randomly in the sky. So we expect the global relation of $C_{\text{sample}} = 0.9999 C_{\text{BOSS}}$ could be also satisfied locally. Therefore, for convenience, we adopt C_{BOSS} for C_{sample} .

We correct the local density estimates for the effects of missing galaxies by using C_{BOSS} and the weight

$$\omega_{\text{tot}} = (\omega_{\text{cp}} + \omega_{\text{rf}} - 1) \omega_{\text{sys}}. \quad (6)$$

ω_{cp} and ω_{rf} are weights for fiber collisions of close pairs and redshift failures respectively. Both of them are assigned one by default, but up-weighted for galaxies that

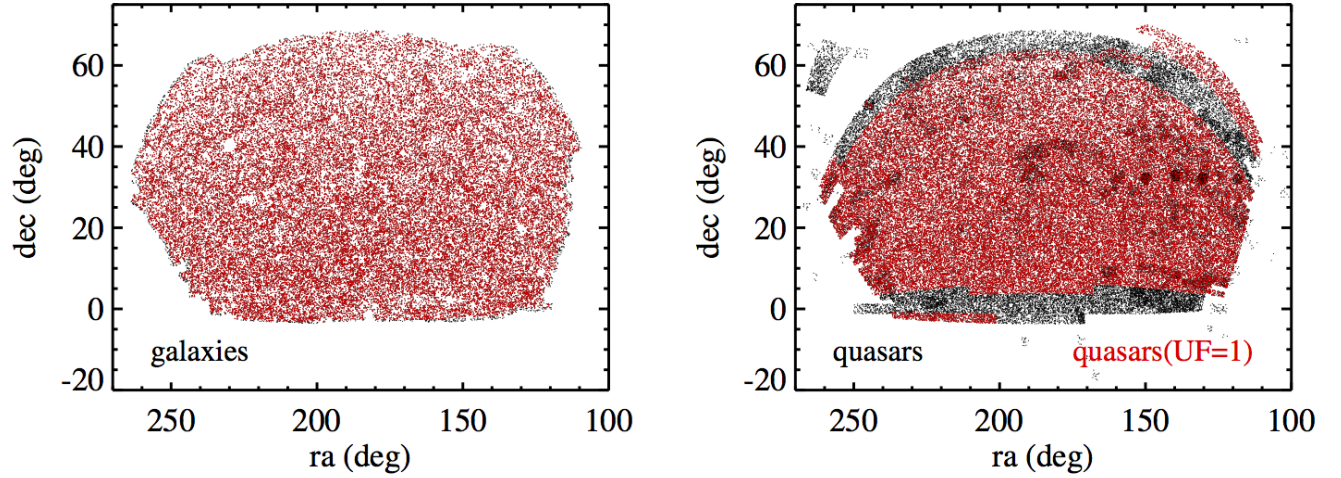


FIG. 1.— Distributions of SDSS-III DR12v4 CMASS galaxies (left) and SDSS DR7 quasars (right) in the northern galactic cap. Only about 10 % of galaxies are shown for clarity. Black dots in both panel represent the full samples. Galaxies within our sample boundaries used to calculate the density field are colored in red. Quasars flagged with $UF = 1$ by Shen et al. (2011) are over-plotted in red in the right panel, and our quasar sample is limited in the middle, largest patch. In our analysis we use the overlapped region of the galaxy and quasar samples.

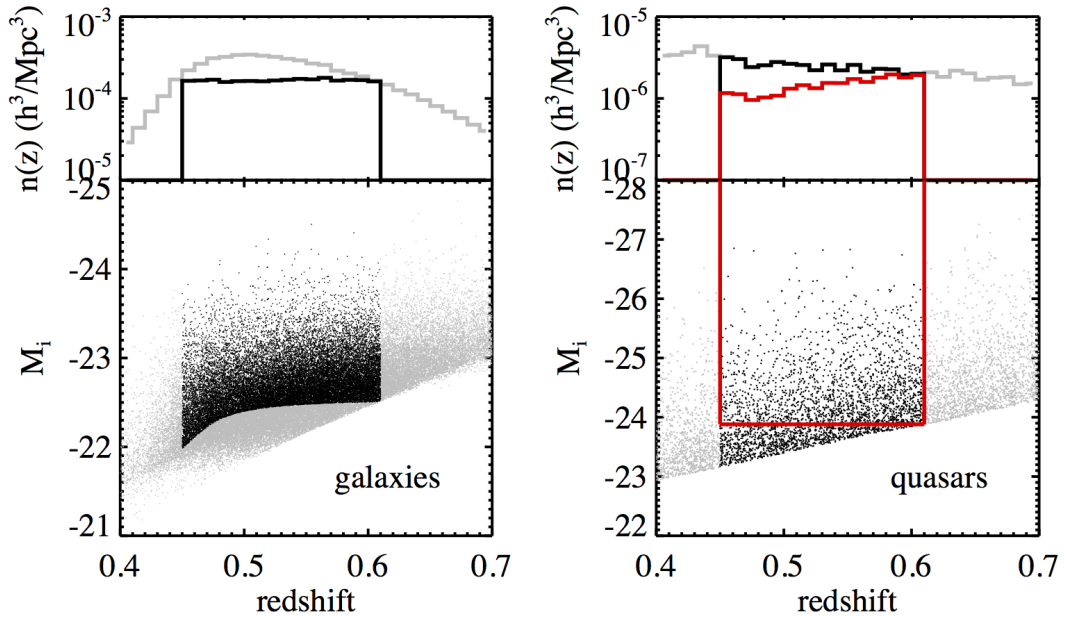


FIG. 2.— Distributions of the SDSS-III CMASS galaxies (left) and SDSS DR7 quasars (right) in the i -band absolute magnitude in redshift space with (comoving) number density histograms as a function of redshift above. Black dots represent those selected for the analysis of this paper. The absolute magnitude cut given by Equation (1) is applied to the galaxy sample to make a constant number density sample with the mean galaxy separation of $17.1 h^{-1} \text{Mpc}$ over the redshift range $0.45 < z < 0.61$. Only about 10 % of galaxies are plotted. All quasars in the redshift range of $0.45 < z < 0.61$ are shown in black. When we study the redshift evolution of quasar properties, a constant absolute magnitude cut of $M_i < -23.9$, shown with the red line, is used for quasars.

have colliding targets of same type (galaxy) and objects with failed redshift as nearest neighbors respectively. ω_{sys} takes into account the spurious fluctuations in galaxy distribution caused by distribution of stars, galactic extinction, seeing, airmass and sky background (imaging systematics). See Anderson et al. (2014) and Ross et al. (2012) for more information about the weights and the completeness. The resulting total weight to each galaxy is $\omega_{\text{fin}} = \omega_{\text{tot}}/C_{\text{BOSS}}$. When the local density is calculated at each cell, instead of fixing N_{nn} to 20, we search for the largest N_{nn} that satisfies

$$\sum_{i=1}^{N_{\text{nn}}} \omega_{i,\text{fin}} < 21. \quad (7)$$

Then the density is calculated from

$$\rho_{20} = \frac{1}{\pi h_{\text{spl}}^3} \sum_{i=1}^{N_{\text{nn}}} W(r_i, h_{\text{spl}}) \omega_{i,\text{fin}}. \quad (8)$$

For the analysis of dependence of quasar properties on background galaxy density, we calculate Equation (8) at the position of each quasar instead of assigning the density at the center of a cell, because the quasars are not always located at their cell center.

3.2. Dealing with boundary effects

When the smooth local density is estimated, care should be taken on the effects of sample boundaries made by the survey definition and screened regions. At each cell we count the number of ‘active’ cells within the distance of $2h_{\text{spl}}$ that belong to the sample volume, and calculate the ratio of the volume occupied by these ‘active’ cells to the volume of the sphere of radius $2h_{\text{spl}}$. The density estimate is corrected by the factor given by the inverse of the ratio. When the ratio is less than 0.8, we discard the cell (about 4%) to guarantee high quality density estimation with insignificant shot noise effects.

While dealing with the boundary effects, cells having low density values are preferentially discarded, thus it causes artificial, secondary boundary effects. It especially results in fake shortages of low-density-cells near the both ends of the redshift range we chose ($0.45 < z < 0.61$). Since we are going to analyze redshift dependence of quasar properties with density, we exclude these artifacts near the redshift boundary by limiting redshift range to be $0.46 < z < 0.59$.

Figure 3 shows the distribution of h_{spl} at the cells selected after the boundary effects are taken into account. h_{spl} typically has a value of $15.2 h^{-1}\text{Mpc}$ and a dispersion of about $2.65 h^{-1}\text{Mpc}$. Figure 4 shows the galaxy number density fields in two thin slices. The map on the left is a slice at $z = 0.5$ with width of $\Delta z = 0.01$ projected on the sky, and the right one is a slice with $7^\circ < \delta < 9^\circ$ projected in the x-y plane of the equatorial coordinate system.

4. RESULTS

4.1. Quasar phenomenon versus galaxy density

In this section we will present our main results on the probability of finding quasars when the local galaxy number density is given. Figure 5 compares the distribution

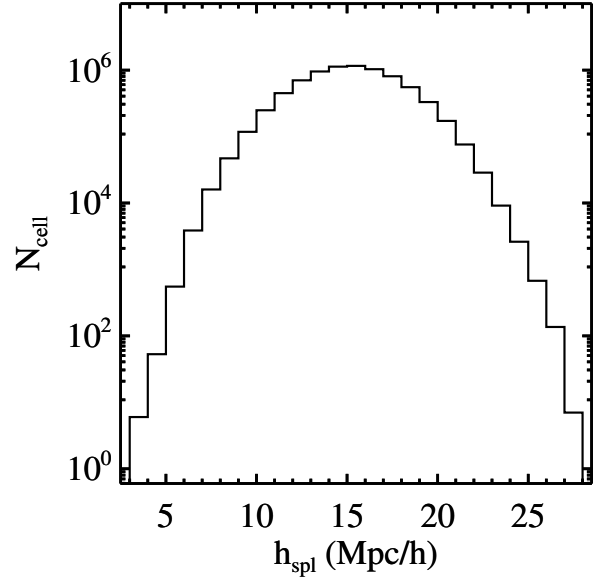


FIG. 3.— Frequency of the smoothing kernel size h_{spl} used to calculate the local galaxy number density.

of galaxies (black dots) with that of quasars (red crosses) in a thin stripe at $z = 0.604$ with width of $\Delta z = 0.01$. The LSSs are not well-traced by them because both samples are sparse. Nevertheless, it can be noticed that two distributions are correlated. The correlation is not strong as evidenced by a few quasars located at empty regions and by high-density regions with no quasars.

Figure 6 shows the number of density cells (black histogram) having the local galaxy density given by the x-axis. The red histogram is the number of quasars whose local density belongs to each density bin. The quasar number density is calculated from $N_{\text{quasar}}/N_{\text{cell}}V_{\text{cell}}$ in each bin of galaxy number density. N_{cell} is the number of cells in a given galaxy density bin and N_{quasar} is the number of quasars contained within those cells. V_{cell} is the volume of a cell, $125 (h^{-1}\text{Mpc})^3$. Figure 7 shows that the quasar number density is monotonically proportional to the background galaxy number density over the whole density range from $\sim 5 \times 10^{-2}$ to $\sim 2 \times 10^1$ times the mean density. The probability of finding quasars increases by more than an order of magnitude over this interval. The error bars are estimated with eight subsamples having one-eighth of the survey area on the sky⁶. The best linear fit shown by a solid line is

$$\log n_Q / (h^3 / \text{Mpc}^3) = \alpha + \beta \log \rho_{20} / \bar{\rho}_{20} \quad (9)$$

with $\alpha = -5.57 \pm 0.02$ and $\beta = 0.618 \pm 0.034$. The slope β is smaller than 1, meaning that quasar density changes slower than galaxy density does. There is a hint for weaker correlation in low-density region. Our result is qualitatively consistent with Shen et al. (2013)’s find-

⁶ The error of quasar number density estimation at i -th background density bin is calculated as $\sigma_i^2 = \frac{1}{N(N-1)} \sum_{k=1}^N (x_{i,k} - \bar{x}_i)^2$ where N is the number of subsamples, $x_{i,k}$ is the measurement from subsample k , and \bar{x}_i is the mean of the measurements from all subsamples.

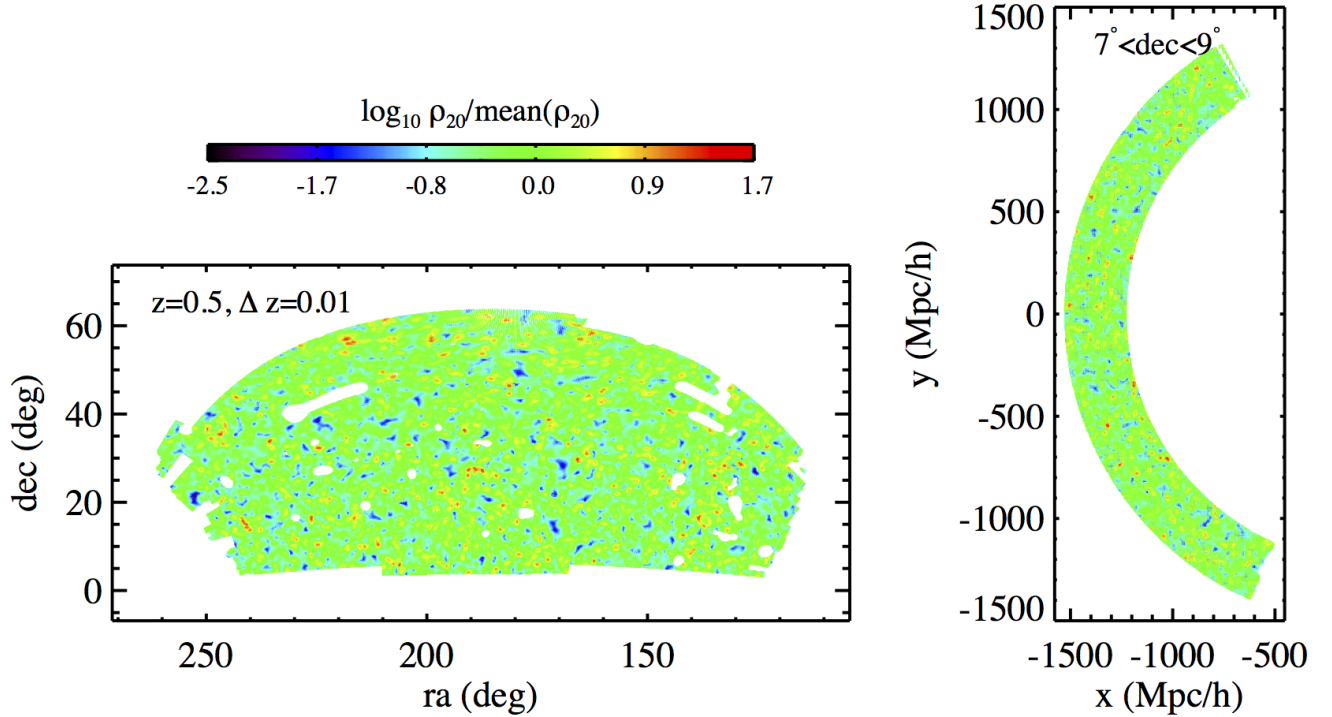


FIG. 4.— (Left) The galaxy density map in a thin slice at a median redshift of 0.5 with width of 0.01 projected on the plane of RA and Dec. (Right) The density map in a thin slice with $7^\circ < \text{Dec} < 9^\circ$ projected into two-dimensional comoving Cartesian space.

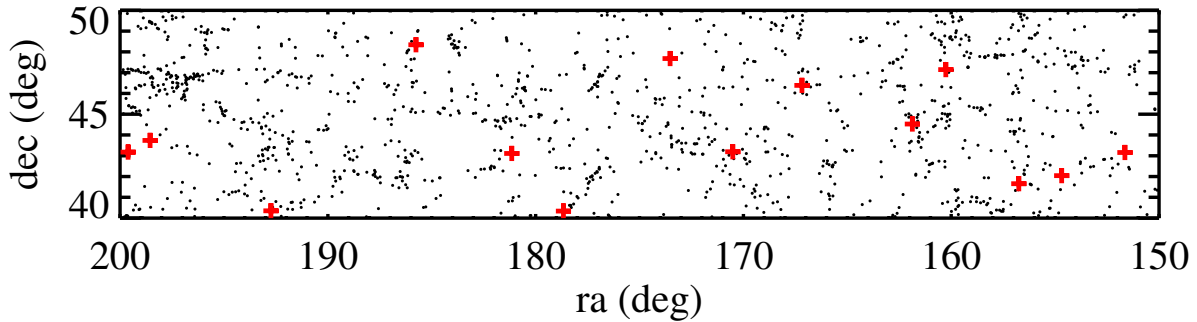


FIG. 5.— Quasars (red crosses) are shown on top of galaxy (black dots) distribution in a stripe at a median redshift of 0.604 and with width of 0.01.

ing that clustering of quasars is positively correlated with that of CMASS galaxies. To perform a quantitative comparison, we need an auto-CF of CMASS galaxies additionally and also the conversion between two-dimensional (Shen et al. 2013) and three-dimensional (this paper) quantities. Also with the 2PCCF of Shen et al. (2013) one can explore only down to regions of mean density, which is a smaller range than what we consider here. So, we simply note that the gentle slope of the relation between quasar and galaxy densities we found can be also inferred from Figure 5 of Shen et al. (2013). To draw this point, we use the relation $n(r) = n_b(1 + \xi_{ab}(r))$ where $n(r)$ is the mean density of b -type objects at distance r from a -type, n_b is the mean number density of b -type

objects, and ξ_{ab} is the CCF of a -type and b -type objects (Peebles 1980, Equation (44.4)). We apply this equation to our case by setting $a = \text{galaxy}$, $b = \text{quasar}$ for quasar-galaxy CCF and $a = b = \text{galaxy}$ for galaxy ACF. The galaxy ACF decreases more rapidly than the quasar-galaxy CCF (Figure 5 of Shen et al. 2013). Therefore, as a function of increasing distance r from a galaxy, the mean density of galaxies decreases rapidly with r than the mean density of quasars does.

We also examine if the relation between quasar density and galaxy density changes with redshift or not. In this particular study we use a quasar sample defined by a uniform absolute magnitude cut of M_i . We divide the sample volume into 3 sub-volumes with redshift ranges of

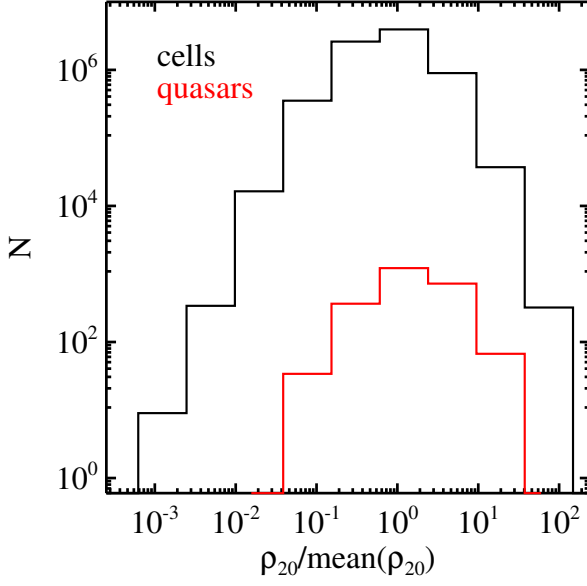


FIG. 6.— The numbers of cells (black) and quasars (red) whose local density belongs to each density bin.

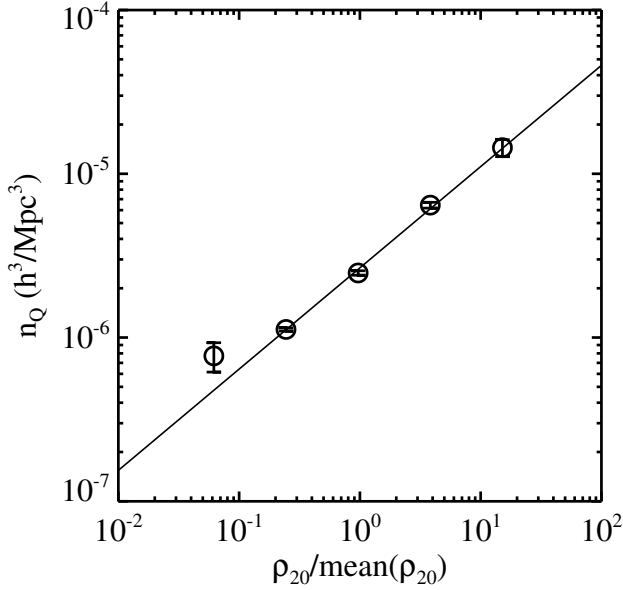


FIG. 7.— Quasar number density as a function of galaxy density. Error bars are calculated from the subsample-to-subsample variation. The solid line is the best linear fit. The mean quasar number density is $2.45 \times 10^{-6} (h^{-1}\text{Mpc})^{-3}$.

$0.46 < z < 0.52$ (low- z), $0.52 < z < 0.56$ (intermediate- z) and $0.56 < z < 0.59$ (high- z). The 3 sub-volumes contain the same number of quasars. In Figure 8 the relations found in the low- z and high- z subsamples are compared. Since the mean number density of quasars brighter than M_i is different for those subsamples, the quasar number density is normalized by its mean value in each subsample. Best fits for the both cases are calculated and drawn in the figure, and as comparison a

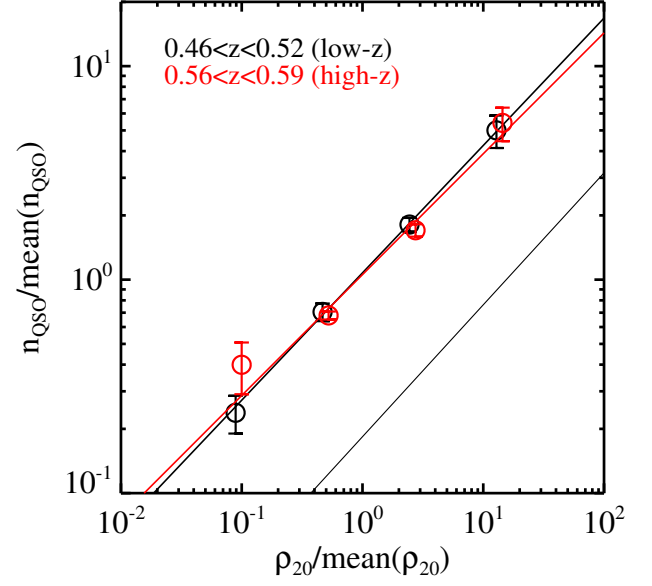


FIG. 8.— Same as 7, quasar density is calculated as a function of galaxy density, but separately for two redshift-subsamples, low (black) and high (red) redshift subsamples. Solid lines in black and red drawn together with circles are best fits respectively. The thinner solid line in right bottom side of the figure having the same slope with the best fit in Figure 7 (Equation (9)) is drawn for comparison.

solid line having the same slope of Equation (9) is also added. It is found that the relations are consistent with each other and redshift evolution of the relation is not detected. Figure 11 of Shen et al. (2013) which summarizes the results of previous 2PCF studies for quasars and galaxy, showing no change in biases of quasar and galaxy in the redshift range similar to ours. It means that there is no redshift evolution of quasar density-galaxy density relation in the given redshift range. Since there is no galaxy bias measurement at a higher redshift to compare with quasar bias, it is difficult to say if the density relation will change or not in a wider redshift range. Further study is needed over a wider redshift range (see 4th paragraph in Section 5 for more discussion).

4.2. Quasar properties as a function of galaxy density

We examine how quasar properties such as bolometric luminosity (L_{bol}), black hole mass ($M_{\text{BH,vir}}$) Eddington ratio (λ) and differential color ($\Delta(g-i)$) depend on background galaxy density. As mentioned in Section 3.1, the galaxy density is calculated in the same way as described in Section 3, but at the position of each quasar. $M_{\text{BH,vir}}$ is the adopted fiducial virial black hole mass calculated by Shen et al. (2011). $\Delta(g-i)$ is given by $(g-i)_{\text{QSO}} - \langle (g-i) \rangle_{\text{redshift}}$ where $\langle (g-i) \rangle_{\text{redshift}}$ is a representative color at the redshift of a quasar which is derived from a well-known tight color-redshift correlation of quasars (Richards et al. 2001, 2003; Schneider et al. 2007). So $\Delta(g-i)$ can tell whether or not an object has a redder or bluer continuum than the typical quasar at the same redshift. All the quasar property parameters are given by Schneider et al. (2010) and Shen et al. (2011). We exclude some quasars with missing informa-

tion from our analysis. These quasars are mainly at high redshift or intrinsically faint, which may have affected the quality of observation.

We bring one more quantity, R_{FeII} , which is the ratio between equivalent widths of the Fe line within $4435 - 4685 \text{ \AA}$ (EW_{FeII}) and broad $\text{H}\beta$ line ($EW_{\text{H}\beta}$). It is known as a good probe of black hole mass (Shen & Ho 2014). The black hole mass provided by Shen et al. (2011) is a derived quantity determined from a number of measurements and based on some assumptions, while R_{FeII} is a single measured quantity and so will suffer from fewer systematic and statistical uncertainties (Shen et al. 2011; Shen & Ho 2014).

We show the scatter plot of M_i of all quasars with respect to local galaxy density in the top left panel of Figure 9. We inspect the dependence of quasar properties across three density bins where statistics is high as shown by the number of quasars in the top right panel. The error bars in black are the standard error of the mean and red error bars above those in black are measurement errors from Shen et al. (2011). As shown in the remaining panels of Figure 9 the changes of the properties with galaxy density are small, and the quasar properties depend only weakly on density. However, due to the good statistics of our sample the dependence on galaxy density is clearly detected for some quasar properties such as M_i , L_{bol} , $M_{\text{BH,vir}}$, R_{FeII} and λ . We find that luminosity (M_i , L_{bol}) decreases with galaxy density, while black hole mass ($M_{\text{BH,vir}}$, R_{FeII}) increases. With such dependence of luminosity and black hole mass, Eddington ratio (λ) decreases with galaxy density. No significant change is detected for color ($\Delta(g-i)$).

5. DISCUSSION

The best-fit linear function of quasar density-galaxy density relation has a slope of 0.618, which means that quasar density changes slower than galaxy density does. It is emphasized even more with the offset of the first point from the linear relation in Figure 7. In under-dense region, quasar incidence is higher than what is expected from the trend in denser regions. This seems consistent with literatures. Even though the detail depends on how AGN are selected (for example in the optical, X-ray, infrared, or radio), the general trend that the AGN fraction in over-dense regions is lower than that in under-dense regions has been identified by a number of studies (Best 2004; Martini et al. 2002, 2006, 2007; Arnold et al. 2009; Hwang et al. 2012; Shen et al. 2007a). These works found that AGN fraction in galaxy groups and poor-to-moderate richness galaxy clusters is higher than that in rich clusters, and AGN fraction is higher in field than clusters. It has been also confirmed that this difference is not simply caused by the morphological mix of galaxies between environments, by examining AGN fractions in different environments using only early-type galaxies (Arnold et al. 2009; Hwang et al. 2012).

As an analogous quantity to the AGN fraction, we calculate the quasar-to-normal galaxy ratio, defined as number of quasars divided by number of CMASS galaxies in a given bin of galaxy density. To be fair and precise, we should prepare quasars and galaxies from an identical parent sample with the same luminosity cut applied. However, it is challenging to prepare such samples from

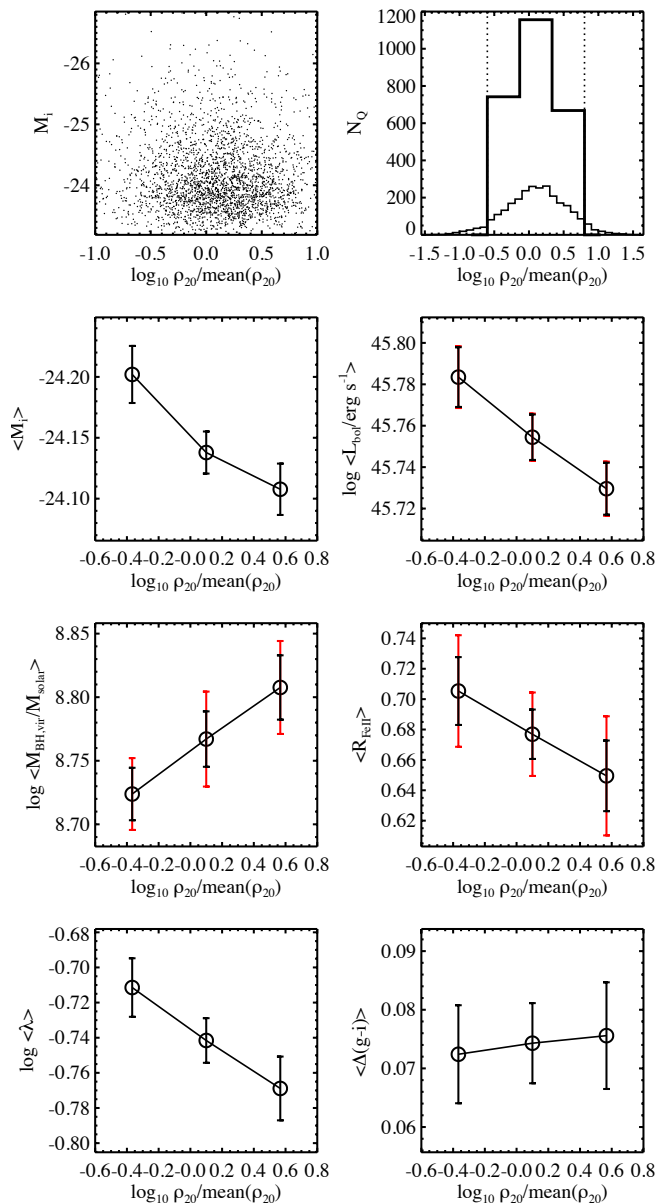


FIG. 9.— (Top, left) Scatter plot of quasars in the plane of M_i and local density. (Top, right) Numbers of quasars in three bins of local density. The three bins have the same width in log scale. (Rest) Averaged value of each quasar property in each bin is shown with error bars. Black error bars are the standard error of the mean and red ones are the measurement error. The quasar properties considered here are absolute i -band magnitude (M_i), bolometric luminosity (L_{bol}), black hole mass ($M_{\text{BH,vir}}$), equivalent width ratio of Fe line and broad $\text{H}\beta$ line (R_{FeII}), Eddington ratio (λ), and differential color ($\Delta(g-i)$).

existing heterogeneous survey data. Instead, as a quick analysis, we use the data we have used in this work. Luminosity cut is separately applied to the two samples since luminosity is calculated at different K-correction redshifts. We impose $M_i < -23.9$ to the quasar sample, while we adopt two magnitude cuts, $M_i < -22.5$ and $M_i < -22.8$, for the galaxy sample. The two magnitude cuts of the galaxy sample are considered to show the trend of the ratio does not change with the magnitude cut, thus compensating the arbitrary and inconsistent

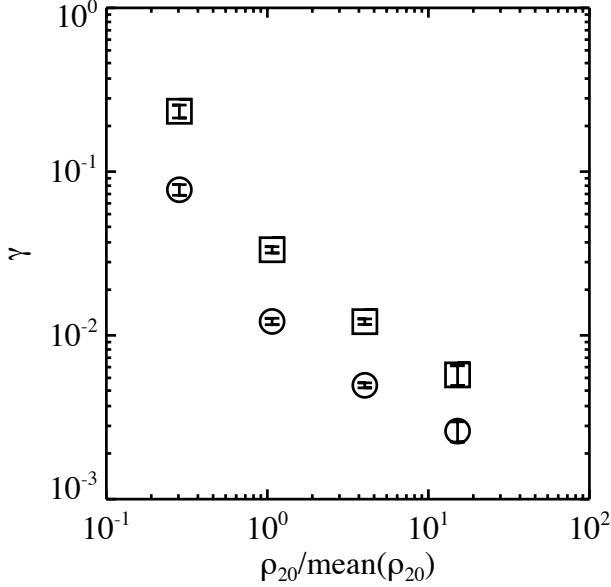


FIG. 10.— Quasar-to-normal galaxy ratio (γ) as a function of galaxy density. At a given galaxy density, number of the quasars of $M_i < -23.9$ divided by number of the CMASS galaxies of $M_i < -22.5$ (circle) or of $M_i < -22.8$ (square). Galaxy density bins are the same with one in Figure 7, but the most under-dense region bin does not appear in this plot since there is no CMASS galaxy in that bin by definition. Error bars are calculated in the same way with the error bars in Figure 7.

choice of luminosity thresholds.

Figure 10 shows that the quasar-to-normal galaxy ratio (γ) decreases as one goes to denser regions. Despite different sample criteria (quasars vs. AGN), different physical quantities (ratio vs. fraction), and different measures of environment (local galaxy density vs. clustercentric radius/velocity dispersion of a system) the results of the literatures and us agree on that AGN phenomenon seems to exhibit more efficiently in under-dense region than in over-dense region. Galaxies in under-dense region tend to have richer cold gas reservoirs than those in over-dense region (Davies & Lewis 1973; Solanes et al. 2001; di Serego Alighieri et al. 2007; Grossi et al. 2009; Cortese et al. 2011; Catinella et al. 2013). In such circumstance, the central engine of AGN-host galaxies in under-dense region may be fueled more sufficiently and be more likely in quasar mode, resulting in a larger fraction of galaxies being observed as quasars. A similar trend was already shown by Best (2004) with lack of emission line AGN in clusters, which is also explained well by lack of cold gas in clusters.

However, the anti-correlation between AGN fraction and environment does not hold at higher redshift such as $z > 1$ (Martini et al. 2013). AGN fraction in clusters evolves so rapidly with redshift (Eastman et al. 2007; Galametz et al. 2009; Martini et al. 2009) that AGN fractions in the field and clusters become consistent at $1 < z < 1.5$. Studies at higher redshifts like $z > 2$ (Lehmer et al. 2009; Digby-North et al. 2010) even show a reversal of the anti-correlation. Based on these studies, we can expect that the linear relation between quasar density and galaxy density we found may also evolve with redshift to have a steeper slope at a higher red-

shift. It might imply that quasars can be used as an efficient probe of dense environment such as protoclusters at high redshifts. Orsi et al. (2015) performed a numerical study of protoclusters associated with radio galaxies and quasars at $2 < z < 6$, and studied their connection to present-day cluster descendants. By finding high- z protoclusters with high- z quasars, the connection can be studied observationally.

The dependence of quasar properties on galaxy density seen in Figure 9 is understood in the frame of hierarchical merging scenario with taking into account the trend of cold gas reservoir of a galaxy with environment aforementioned. A galaxy in denser environment has experienced more mergers and interactions, thus its central engine, supermassive black hole (SMBH), is heavier, which is seen from the trend of $M_{\text{BH,vir}}$ and R_{FeII} . Decreasing trend of the average quasar luminosity (M_i , L_{bol}) and activity (λ) with galaxy density is due to the lack of fuel (cold gas) to feed the SMBH in denser environment, even though quasars in denser region have deeper gravitational potential by more massive SMBH to drag fuel more effectively.

Similar, but stronger dependence of properties such as color and star formation rate (SFR) on environment have been observed in galaxies as well, and the dependence reflect the amount of cold gas in different environments (e.g., Hashimoto et al. 1998; Kauffmann et al. 2004; Skibba et al. 2009). Wijesinghe et al. (2012) found that the SFR-density relation at $z < 0.2$ is visible when both passive and star-forming galaxy populations are considered, while it is not seen when looking at the star-forming population only. It might indicate that at that redshift range the primary effect of environment on galaxy properties comes from gas removal process rather than gas supply process. Both star formation and AGN activities depend to the first order on the presence of cold gas. One could therefore expect environmental effects acting on cold gas to produce similar environmental trends in both star-forming and AGN populations. However, the gas directly feeding star formation is distributed differently than the one powering the AGN (on larger scales vs. more centrally concentrated). The SMBH feeding process is also expected to be stochastic (Hopkins & Hernquist 2006; Peng 2007; Jahnke & Macciò 2011; Hickox et al. 2014). As a consequence, the fuel of the AGN will tend to be better shielded against environmental effects than that of star formation, which might be transferred into weak dependence of quasar properties on environment.

Meanwhile quasar clustering studies with CFs have reported weakly positive correlation between quasar luminosity and host DMH mass (Adelberger & Steidel 2005; Croom et al. 2005; Lidz et al. 2006; Coil et al. 2007; Hopkins et al. 2007; Myers et al. 2007; Krumpke et al. 2010, 2012; Shen et al. 2013). They found that more luminous quasars reside in marginally more massive DMHs, which appears to reflect the opposite trend that we find here. However, both effects are relatively weak, and the difference may be due to the fact that we are taking the opposite approach to clustering studies for connecting quasar properties to large-scale environment. Our results appear to follow the well-established trends observed for the amount cold gas as a function of environment, and so

may provide a useful clue with regards to quasar fueling.

6. CONCLUSION

In this paper, we construct a galaxy number density field using the SDSS DR12 CMASS catalog and study how galaxy density affects the SDSS DR7 quasar properties. The relation between quasar density and galaxy density is well described with a linear function for logarithmic densities. Quasars show weak dependence of their properties on environment: SMBH mass increases with galaxy density, while luminosity decreases. It should be noted that the linear relation between quasar density and galaxy density can make quasars a good tracer of LSSs of the universe at high redshifts where quasar are observed more easily than galaxies. The relation makes it possible to trace the LSSs in the galaxy distribution directly from observed quasars. We do not detect any redshift dependence of the relation in the narrow redshift range we use. However, as discussed above, a redshift evolution of the relation between quasar density and galaxy density is expected – quasars trace overdense region more sensitively, thus quasars can be a good marker of protoclusters at high redshift. Moreover, the weak dependence of quasar properties on galaxy density reinforces our argument that quasars can trace the LSSs at different redshifts when the quasar properties might change systematically. However, as mentioned before, since the redshift range we consider in this study is narrow, a further study with a wider redshift range is needed to confirm the weak dependence.

The authors thank the referee for thorough report. It helped to improve the presentation of this work. The authors thank Korea Institute for Advanced Study

for providing computing resources (KIAS Center for Advanced Computation Linux Cluster System). H. Lietzen acknowledges financial support from the Spanish Ministry of Economy and Competitiveness (MINECO) under the 2011 Severo Ochoa Program MINECO SEV-2011-0187. M. Einasto is supported by the ETAG project IUT26-2 of the Estonian Ministry of Education and Research and by the project TK133, financed by the European Union through the European Regional Development Fund. H. Song thanks R. Gobat for his helpful comments on this work.

Funding for SDSS-III has been provided by the Alfred P. Sloan Foundation, the Participating Institutions, the National Science Foundation, and the U.S. Department of Energy Office of Science. The SDSS-III web site is <http://www.sdss3.org/>.

SDSS-III is managed by the Astrophysical Research Consortium for the Participating Institutions of the SDSS-III Collaboration including the University of Arizona, the Brazilian Participation Group, Brookhaven National Laboratory, Carnegie Mellon University, University of Florida, the French Participation Group, the German Participation Group, Harvard University, the Instituto de Astrofísica de Canarias, the Michigan State/Notre Dame/JINA Participation Group, Johns Hopkins University, Lawrence Berkeley National Laboratory, Max Planck Institute for Astrophysics, Max Planck Institute for Extraterrestrial Physics, New Mexico State University, New York University, Ohio State University, Pennsylvania State University, University of Portsmouth, Princeton University, the Spanish Participation Group, University of Tokyo, University of Utah, Vanderbilt University, University of Virginia, University of Washington, and Yale University.

REFERENCES

- Adelberger, K. L., & Steidel, C. C. 2005, *ApJ*, 630, 50
 Alam, S., Albareti, F. D., Allende Prieto, C., et al. 2015, *ApJS*, 219, 12
 Allevato, V., Finoguenov, A., Civano, F., et al. 2014, *ApJ*, 796, 4
 Anderson, L., Aubourg, É., Bailey, S., et al. 2014, *MNRAS*, 441, 24
 Arnold, T. J., Martini, P., Mulchaey, J. S., Berti, A., & Jeltema, T. E. 2009, *ApJ*, 707, 1691
 Best, P. N. 2004, *MNRAS*, 351, 70
 Bolton, A. S., Schlegel, D. J., Aubourg, É., et al. 2012, *AJ*, 144, 144
 Cannon, R., Drinkwater, M., Edge, A., et al. 2006, *MNRAS*, 372, 425
 Cappelluti, N., Allevato, V., & Finoguenov, A. 2012, *Advances in Astronomy*, 2012, 853701
 Catinella, B., Schiminovich, D., Cortese, L., et al. 2013, *MNRAS*, 436, 34
 Chen, Y.-M., Kauffmann, G., Tremonti, C. A., et al. 2012, *MNRAS*, 421, 314
 Clowes, R. G., Harris, K. A., Raghunathan, S., et al. 2013, *MNRAS*, 429, 2910
 Coil, A. L., Hennawi, J. F., Newman, J. A., Cooper, M. C., & Davis, M. 2007, *ApJ*, 654, 115
 Cortese, L., Catinella, B., Boissier, S., Boselli, A., & Heinis, S. 2011, *MNRAS*, 415, 1797
 Croom, S. M., Smith, R. J., Boyle, B. J., et al. 2004, *MNRAS*, 349, 1397
 Croom, S. M., Boyle, B. J., Shanks, T., et al. 2005, *MNRAS*, 356, 415
 Davies, R. D., & Lewis, B. M. 1973, *MNRAS*, 165, 231
 Dawson, K. S., Schlegel, D. J., Ahn, C. P., et al. 2013, *AJ*, 145, 10
 di Serego Alighieri, S., Gavazzi, G., Giovanardi, C., et al. 2007, *A&A*, 474, 851
 Digby-North, J. A., Nandra, K., Laird, E. S., et al. 2010, *MNRAS*, 407, 846
 Djorgovski, S. G. 1999, in *Astronomical Society of the Pacific Conference Series*, Vol. 193, *The Hy-Redshift Universe: Galaxy Formation and Evolution at High Redshift*, ed. A. J. Bunker & W. J. M. van Breugel, 397
 Djorgovski, S. G., Bogosavljevic, M., & Mahabal, A. 2006, *New A Rev.*, 50, 140
 Djorgovski, S. G., Stern, D., Mahabal, A. A., & Brunner, R. 2003, *ApJ*, 596, 67
 Eastman, J., Martini, P., Sivakoff, G., et al. 2007, *ApJ*, 664, L9
 Eftekharzadeh, S., Myers, A. D., White, M., et al. 2015, *MNRAS*, 453, 2779
 Einasto, M., Tago, E., Lietzen, H., et al. 2014, *A&A*, 568, A46
 Eisenstein, D. J., Annis, J., Gunn, J. E., et al. 2001, *AJ*, 122, 2267
 Eisenstein, D. J., Weinberg, D. H., Agol, E., et al. 2011, *AJ*, 142, 72
 Galametz, A., Stern, D., Eisenhardt, P. R. M., et al. 2009, *ApJ*, 694, 1309
 Grossi, M., di Serego Alighieri, S., Giovanardi, C., et al. 2009, *A&A*, 498, 407
 Gunn, J. E., Siegmund, W. A., Mannery, E. J., et al. 2006, *AJ*, 131, 2332
 Han, D.-H., & Park, M.-G. 2015, *Journal of Korean Astronomical Society*, 48, 83
 Hashimoto, Y., Oemler, Jr., A., Lin, H., & Tucker, D. L. 1998, *ApJ*, 499, 589
 Hickox, R. C., Mullaney, J. R., Alexander, D. M., et al. 2014, *ApJ*, 782, 9
 Hopkins, P. F., & Hernquist, L. 2006, *ApJS*, 166, 1
 Hopkins, P. F., Lidz, A., Hernquist, L., et al. 2007, *ApJ*, 662, 110
 Hutsemékers, D., Braibant, L., Pelgrims, V., & Sluse, D. 2014, *A&A*, 572, A18
 Hwang, H. S., Park, C., Elbaz, D., & Choi, Y.-Y. 2012, *A&A*, 538, A15
 Jahnke, K., & Macciò, A. V. 2011, *ApJ*, 734, 92
 Jennen-Steinmetz, C., & Gasser, T. 1988, 83, 1084

- Kauffmann, G., White, S. D. M., Heckman, T. M., et al. 2004, *MNRAS*, 353, 713
- Krumpe, M., Miyaji, T., & Coil, A. L. 2010, *ApJ*, 713, 558
- Krumpe, M., Miyaji, T., Coil, A. L., & Aceves, H. 2012, *ApJ*, 746, 1
- Krumpe, M., Miyaji, T., Husemann, B., et al. 2015, *ApJ*, 815, 21
- Laigle, C., Pichon, C., Codis, S., et al. 2015, *MNRAS*, 446, 2744
- Lehmer, B. D., Alexander, D. M., Geach, J. E., et al. 2009, *ApJ*, 691, 687
- Lidz, A., Hopkins, P. F., Cox, T. J., Hernquist, L., & Robertson, B. 2006, *ApJ*, 641, 41
- Lietzen, H., Heinämäki, P., Nurmi, P., et al. 2011, *A&A*, 535, A21
- . 2009, *A&A*, 501, 145
- Lietzen, H., Tempel, E., Liivamägi, L. J., et al. 2016, *A&A*, 588, L4
- Maraston, C., Pforr, J., Henriques, B. M., et al. 2013, *MNRAS*, 435, 2764
- Martini, P., Kelson, D. D., Kim, E., Mulchaey, J. S., & Athey, A. A. 2006, *ApJ*, 644, 116
- Martini, P., Kelson, D. D., Mulchaey, J. S., & Trager, S. C. 2002, *ApJ*, 576, L109
- Martini, P., Mulchaey, J. S., & Kelson, D. D. 2007, *ApJ*, 664, 761
- Martini, P., Sivakoff, G. R., & Mulchaey, J. S. 2009, *ApJ*, 701, 66
- Martini, P., Miller, E. D., Brodwin, M., et al. 2013, *ApJ*, 768, 1
- Miyaji, T., Krumpe, M., Coil, A. L., & Aceves, H. 2011, *ApJ*, 726, 83
- Momjian, E., Carilli, C. L., Walter, F., & Venemans, B. 2014, *AJ*, 147, 6
- Monaghan, J. J. 1992, *ARA&A*, 30, 543
- Monaghan, J. J., & Lattanzio, J. C. 1985, *A&A*, 149, 135
- Mortlock, D. J., Warren, S. J., Venemans, B. P., et al. 2011, *Nature*, 474, 616
- Myers, A. D., Brunner, R. J., Nichol, R. C., et al. 2007, *ApJ*, 658, 85
- Nadathur, S. 2013, *MNRAS*, 434, 398
- Orsi, A. A., Fanidakis, N., Lacey, C. G., & Baugh, C. M. 2015, *ArXiv e-prints*, arXiv:1509.01254
- Park, C., Song, H., Einasto, M., Lietzen, H., & Heinämäki, P. 2015, *Journal of Korean Astronomical Society*, 48, 75
- Peebles, P. J. E. 1980, *The large-scale structure of the universe*
- Pelgrims, V., & Hutsemékers, D. 2015, *ArXiv e-prints*, arXiv:1503.03482
- Peng, C. Y. 2007, *ApJ*, 671, 1098
- Richards, G. T., Fan, X., Schneider, D. P., et al. 2001, *AJ*, 121, 2308
- Richards, G. T., Fan, X., Newberg, H. J., et al. 2002, *AJ*, 123, 2945
- Richards, G. T., Hall, P. B., Vanden Berk, D. E., et al. 2003, *AJ*, 126, 1131
- Richards, G. T., Lacy, M., Storrie-Lombardi, L. J., et al. 2006, *ApJS*, 166, 470
- Richardson, J., Zheng, Z., Chatterjee, S., Nagai, D., & Shen, Y. 2012, *ApJ*, 755, 30
- Risaliti, G., & Lusso, E. 2015, *ArXiv e-prints*, arXiv:1505.07118
- Ross, A. J., Percival, W. J., Sánchez, A. G., et al. 2012, *MNRAS*, 424, 564
- Ross, N. P., Shen, Y., Strauss, M. A., et al. 2009, *ApJ*, 697, 1634
- Schneider, D. P., Hall, P. B., Richards, G. T., et al. 2007, *AJ*, 134, 102
- Schneider, D. P., Richards, G. T., Hall, P. B., et al. 2010, *AJ*, 139, 2360
- Shen, Y., & Ho, L. C. 2014, *Nature*, 513, 210
- Shen, Y., Mulchaey, J. S., Raychaudhury, S., Rasmussen, J., & Ponman, T. J. 2007a, *ApJ*, 654, L115
- Shen, Y., Strauss, M. A., Oguri, M., et al. 2007b, *AJ*, 133, 2222
- Shen, Y., Strauss, M. A., Ross, N. P., et al. 2009, *ApJ*, 697, 1656
- Shen, Y., Richards, G. T., Strauss, M. A., et al. 2011, *ApJS*, 194, 45
- Shen, Y., McBride, C. K., White, M., et al. 2013, *ApJ*, 778, 98
- Skibba, R. A., Bamford, S. P., Nichol, R. C., et al. 2009, *MNRAS*, 399, 966
- Smee, S. A., Gunn, J. E., Uomoto, A., et al. 2013, *AJ*, 146, 32
- Solanes, J. M., Manrique, A., García-Gómez, C., et al. 2001, *ApJ*, 548, 97
- Tempel, E., Tamm, A., Gramann, M., et al. 2014, *A&A*, 566, A1
- Turner, E. L. 1991, *AJ*, 101, 5
- Wijesinghe, D. B., Hopkins, A. M., Brough, S., et al. 2012, *MNRAS*, 423, 3679
- York, D. G., Adelman, J., Anderson, Jr., J. E., et al. 2000, *AJ*, 120, 1579

APPENDIX

We perform a simple test to estimate the reliability of the smoothed density field when $N_{\text{nn}} = 20$ is used. We place particles at uniformly spaced mesh points to mimic a uniform density field, and measure the density at random spatial points using the Spline kernel smoothing method for various values of N_{nn} . Figure 11 shows the mean and standard deviation of the measured densities as a function of N_{nn} . As N_{nn} increases, the mean density approaches the true value (the solid horizontal line in the left panel of Figure 11) with a smaller standard deviation. $N_{\text{nn}} = 20$ is the smallest value at which the standard deviation drops below 1%. This experiment shows that the error in the smoothed density measure falls below 1% for $N_{\text{nn}} \geq 20$ in the case of the uniform particle distribution. The error for clustered particle distributions depends on the ratio between the clustering scale and mean particle separation for each given N_{nn} . For a clustered distribution, larger uncertainty than 1% is expected, but we checked that even the 10% uncertainty in the galaxy density estimation has less than 1σ effect on the relation between the quasar and galaxy densities found in the paper.

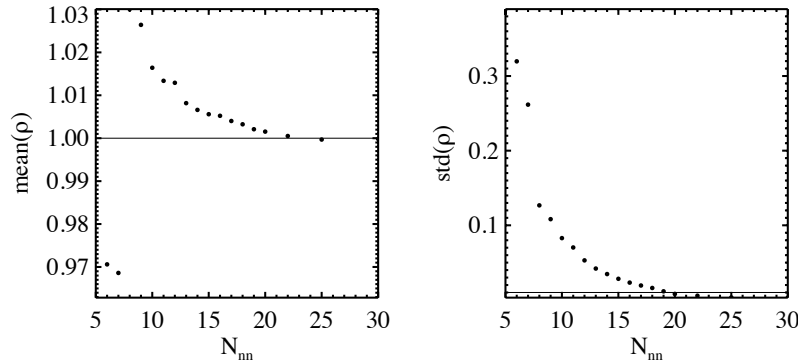


FIG. 11.— (Left) Mean of the densities measured at random spatial points by using the Spline kernel smoothing with the number of the neighbors within the kernel, N_{nn} , varied from 6 to 25. The solid horizontal line represents the true density. (Right) Standard deviation of densities as a function of N_{nn} . Solid horizontal line represents 1% of the density.